PCCP

PAPER

View Article Online
View Journal | View Issue

Check for updates

Cite this: *Phys. Chem. Chem. Phys.*, 2022, **24**, 23195

Interactions of water and short-chain alcohols with $CoFe_2O_4(001)$ surfaces at low coverages†

Arjeta Rushiti, *[a] Tobias Falk,[b] Martin Muhler [b] and Christof Hättig [a]

Received 31st May 2022,
Accepted 6th September 2022

DOI: 10.1039/d2cp02480b

rsc.li/pccp

Iron and cobalt-based oxides crystallizing in the spinel structure are efficient and affordable catalysts for the oxidation of organics, yet, the detailed understanding of their surface structure and reactivity is limited. To fill this gap, we have investigated the (001) surfaces of cobalt ferrite, $CoFe_2O_4$, with the A- and B-layer terminations using density functional theory (DFT/PBE0) and an embedded cluster model. We have considered the five-fold coordinated $Co^{2+/3+}$ (O_h), two-fold coordinated Fe^{2+} (T_d), and an oxygen vacancy, as active sites for the adsorption of water and short-chain alcohols: methanol, ethanol, and 2-propanol, in the low coverage regime. The adsorbates dissociate upon adsorption on the Fe sites whereas the adsorption is mainly molecular on Co. At oxygen vacancies, the adsorbates always dissociate, fill the vacancy and form (partially) hydroxylated surfaces. The computed vibrational spectra for the most stable configurations are compared with results from diffuse reflectance infrared Fourier transform spectroscopy.

Published on 08 September 2022. Downloaded on 10/6/2022 1:29:36 PM.

1 Introduction

Transition metal oxides of the spinel type have emerged as highly efficient and benign heterogeneous catalysts.[1] For instance, iron- and cobalt-based spinels, such as $CoFe_2O_4$ and Co_3O_4, have shown promising catalytic activity as anode materials in electrochemical water splitting,[2,3] in CO oxidation,[4,5] and combustion of volatile organic compounds in the gas phase.[6,7]

Spinel cobalt ferrite, $CoFe_2O_4$ (CFO), is an insulating magnetic oxide with inverse-type face-centered cubic structure. The Fe^{3+} cations are distributed over 1/8 of the tetrahedral interstices (T_d or A-sites), whereas 1/2 of the octahedral interstices (O_h or B-sites) are occupied by Co^{2+} and Fe^{3+}. In the bulk, CFO exhibits Néel-type antiferrimagnetic arrangement with Curie temperature of about T_C = 670 K.[8] Both Co and Fe ions are in high-spin states, such that the magnetic moments of Fe in the T_d and O_h sites are oriented antiparallel to each-other, and the overall net magnetization is attributed to the divalent Co(O_h) cations.[9,10]

An attractive aspect of Fe and Co-based spinels is their affordable cost in comparison to noble metal catalysts. Therefore, they have been intensively studied in recent years as alternative catalysts for total and selective oxidation reactions of organics, which is of significant importance in the chemical industry, in particular, in petrochemistry[11] and fine chemical production.[12] Many experimental studies[13–17] have focused on the selective oxidation of 2-propanol as a probe reaction for investigating mechanistic aspects. For instance, Anke *et al.*[13] explored the interaction of 2-propanol and O_2 with Co_3O_4 surfaces and report nearly full conversion with 100% selectivity to acetone at 430 K. The results are compared with theoretical data which identify the oxidative dehydrogenation as the energetically most favored pathway. Another experimental study[14] addressed the catalytic properties of the $Co_{1+x}Fe_{2-x}O_4$ ($0 \leq x \leq 2$) spinels in a kinetic study for the aerobic oxidation of aqueous 2-propanol solutions, and found that the reaction rate is strongly dependent on the Co^{3+} content. In an attempt to unravel the reactivity of Co_3O_4 towards alcohol oxidation, Lv *et al.*[18] theoretically investigated methanol decomposition on the (110)-B and (111)-B surfaces. Their findings suggest higher oxidation activity for the (110)-B surface with Co^{3+} and the 2-fold coordinated lattice oxygen as active sites.

Despite this progress, concepts relating reaction kinetics of detailed step-by-step sequences of probable mechanisms, the role of surface reactive oxygen species (ROS), oxygen vacancies, and different surface structure and spinel compositions, are still insufficient. Therefore, the main objective of the present work is to explore the adsorption mechanism of water and short-chain alcohols: methanol, ethanol, and 2-propanol on the (001) CFO surfaces in the low coverage regime, as a fundamental step for understanding the catalytic oxidation of alcohols on spinels. Using density functional theory (DFT) and an embedded cluster approach, we investigate the interactions

[a] *Department of Theoretical Chemistry, Ruhr University Bochum, 44780 Bochum, Germany. E-mail: Arjeta.Rushiti@ruhr-uni-bochum.de*
[b] *Laboratory of Industrial Chemistry, Ruhr University Bochum, 44780 Bochum, Germany*

† Electronic supplementary information (ESI) available: Optimized geometries of equilibrium structures and transition states for the adsorbates; determination of scaling factors; calculated vibrational spectra. See DOI: **https://doi.org/10.1039/d2cp02480b**

Published on 08 September 2022. Downloaded on 10/6/2022 1:29:36 PM.

that occur between surface Fe/Co metal sites and an oxygen vacancy with a water or alcohol molecule in the gas phase. We provide energetics and optimized geometries of equilibrium structures for the adsorbates in different molecular and dissociative adsorption conformations as well as optimized structures of transition states. For the dissociatively adsorbed molecules we focus on the O–H bond scission, which has been found to be kinetically more favorable than the C–H and C–O bond cleavages in alcohol decomposition over many metal and metal oxide surfaces,[19–22] including the (110)-B and (111)-B surfaces of Co_3O_4.[18] Furthermore, we compare the computed vibrational signatures of the equilibrium structures with experimental spectra from diffuse reflectance infrared Fourier transform spectroscopy (DRIFTS).

2 Computational details

2.1 Surface models

To theoretically model the (001) CFO surfaces, we used finite sized clusters which were validated in convergence studies of adsorption potentials in a previous study.[23] The quantum mechanically treated clusters have the following stoichiometry: $Co_{10}Fe_{23}O_{42}$, $Co_{18}Fe_{23}O_{52}$, $Co_{22}Fe_{33}O_{80}$, and their structures close to a hemispherical shape are presented in Fig. 1.

The most stable [001] stacking of CFO contains alternating layers of Co and Fe in O_h sites and forms two distinct surface terminations, namely, A and B.[24,25] The B termination contains oxygen and Co(O_h) or Fe(O_h) at the surface layer, whereas the A termination contains an additional monolayer of iron in tetrahedral positions. Here, we focused only on the Co-terminated A and B layers.

Cleaving the bulk CFO in the Co-terminated [001] orientation leads to a decreased coordination for the surface sites and a modification in their oxidation states. As a consequence, iron at the A-layer becomes two-fold coordinated and adopts the oxidation state of +2, whereas cobalt becomes five-fold coordinated and, due to the excess monolayer of Fe, stabilizes in a bulk-like +2 (high-spin) oxidation state.[24] By contrast, the surface five-fold coordinated Co sites at the B-layer adopt a +3 oxidation state with an intermediate spin configuration.[24,26] Since the A-layer is composed of Co^{II} and the B-layer of Co^{III} in similar geometries, we also explore the reactivity of cobalt in two different oxidation states in this study.

The cluster structures in Fig. 1a and b were built symmetrically around the Fe^{II} and Co^{II} active sites at the A-layer, whereas the cluster in Fig. 1c was built symmetrically around the Co^{III} site or an oxygen vacancy at the B-layer.

2.2 Embedded cluster calculations

All calculations were carried out with the periodic electrostatic embedded cluster model (PEECM)[27] as implemented in the TURBOMOLE V7.4 program package.[28] In this approach, the extended solid system is split into three regions: the cluster region, which contains the isolated reaction site in question; the embedding region, which describes the lattice environment by an infinite array of point charges; and the intermediate region, which consists of effective core potentials (ECPs) to prevent artificial polarization of the electron density at the cluster boundary.

We used DFT at the PBE0[29]/def2-SVP[30] level to account for the strongly correlated electrons in CFO. To aid in the computational speed, we applied the resolution of identity approximation for the electronic Coulomb interaction term, with auxiliary basis sets[31] optimized for the corresponding orbital basis sets.

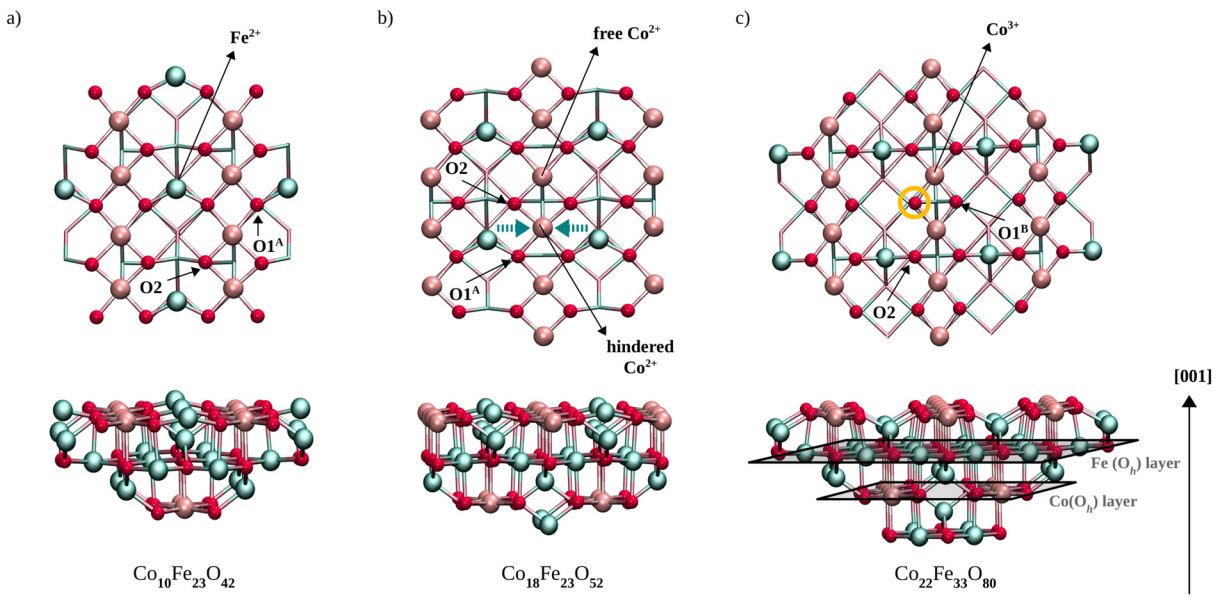


Fig. 1 The most stable stacking of CFO in the [001] direction contains alternating layers of Co and Fe in octahedral sites. Top and side views of the cluster models built symmetrically around the (a) Fe^{II} and (b) Co^{II} active sites at the A-layer and the (c) Co^{III} active site or an oxygen vacancy at the B-layer of the Co-terminated (001) CFO surface. The different types of metal sites and oxygen atoms are defined in the text. The introduced oxygen vacancy is denoted by a yellow circle whereas the green arrows indicate steric hindrance by the proximity of the Fe cations at the A-layer.

 This journal is © the Owner Societies 2022

Published on 08 September 2022. Downloaded on 10/6/2022 1:29:36 PM.

The finite-sized clusters in Fig. 1, modelling the different active sites at the (001)-A and B surfaces of CFO, were treated quantum mechanically in a setup for the embedding which has been evaluated in a previous study.[23] In this embedding setup, the two-dimensional periodic array of point charges was constructed by combining bulk and relaxed surface structures taken from periodic DFT(PBE)+U calculations.[24] For the electrostatic embedding we used full formal ionic charges: 2+ for surface Fe/Co at the A-layer, 3+ for surface Co at the B-layer, 2− for oxygen, and 2+/3+ for bulk Co/Fe. The nearest cations in the embedding around the clusters were augmented with relativistic 28 e^- Zn/Ga ECPs (ecp-28-sdf) from ref. 32 and 33 with similar radii as the $Co^{2+/3+}$ and $Fe^{2+/3+}$ ions.

Optimizations were performed such that only the geometry of the most inner part of the quantum cluster was allowed to relax and adjust to the method and the introduced defects and adsorbates. An initial guess for the transition states was obtained by using the chain-of-state method implemented in the woelfling module[34] of TURBOMOLE, and the transitions states were further refined using the trust-region image minimization (TRIM) algorithm.[35] We used the DFT grid m5 and convergence thresholds of 1×10^{-8} and 1×10^{-3} for the total energy and the maximum norm of the Cartesian energy gradient, respectively. For the self-consistent field (SCF) part we employed the augmented Roothaan–Hall method[36] for optimizing Hartree–Fock and Kohn–Sham density matrices.

Adsorption energies of all equilibrium structures and transition states were determined as the energy differences between the cluster–adsorbate complexes and fully separated structures ($\Delta E_{ads} = E_{cluster+adsorbate} - E_{cluster} - E_{adsorbate}$). They include the zero-point vibrational energy contributions calculated within the harmonic approximation. The Hessian matrix and the dipole gradients for the vibrational frequency calculations were computed by considering the derivatives of the quadrature weights and a numerical differentiation of the gradients, with a stepwidth of 0.02 a.u. for the Cartesian coordinate displacements. For a comparison with the experimental spectra, the computed harmonic frequencies were scaled with factors to correct for the neglect of anharmonicity and systematic errors of the DFT functional and the basis set. Since these empirical correction factors depend on the kind of the normal mode (for instance, CO stretch frequencies need a much lower value than deformation modes), we calculated harmonic frequencies of isolated methanol, ethanol, and 2-propanol in the gas phase and determined individual scaling factors based on the mode type, to best match the experimental measurements. In this way, we obtained average factors of 0.956 for CH, 0.976 for CC, 0.920 for CO, and 0.943 for OH stretching vibrations, and 0.984 for all other normal modes which do not fit to one of these types (see details in ESI†).

3 Experimental methods

In situ DRIFTS measurements were performed in a Nicolet NEXUS™ FT-IR spectrometer equipped with a liquid-nitrogen cooled MCT-A detector and an Ever-Glow mid-IR source. A *PIKE DiffuseIR*™ diffuse reflectance accessory with a *PIKE DiffuseIR*™ high-temperature environmental chamber equipped with a KBr window was used for the DRIFTS measurements. A home-built pressure control system allowed the evacuation of the environmental chamber to a base pressure of 2×10^{-6} mbar. The system consists of a pre-vacuum membrane pump, a turbomolecular pump, and an electronically actuated leak-valve enabling the adjustment of a constant probe molecule pressure up to 1 bar. 20 mg of finely grounded commercial $CoFe_2O_4$ (Sigma-Aldrich) was placed in a porous ceramic crucible. The catalysts were pretreated at 200 °C for 120 min (heating ramp 10 K min^{-1}) in synthetic air (20 sccm, ALPHAGAZ™ 1, Air Liquide) containing 20.5 ± 0.5% O_2 in N_2 and traces of moisture (<2 ppm), hydrocarbons (<0.1 ppm), CO (<1 ppm), and CO_2 (<1 ppm). Afterwards, the environmental chamber was cooled to 30 °C and evacuated until base pressure was reached and background spectra were collected. The probe molecule pressure (methanol, ethanol, and 2-propanol) was stepwise adjusted between 1×10^{-4} mbar and 25 mbar and DRIFT spectra were recorded for each step, respectively. Data collection was performed with a spectral resolution of $\Delta\nu$ = 4 cm^{-1}, 256 scans and an aperture setting of 150. All spectra of the adsorbed probe molecules are presented as log(1/*R*) plots with *R* being the reflectance of the clean sample surface.

4 Results and discussion

4.1 Adsorption at pristine surfaces

On the defect-free A and B terminations of the CFO (001) surface we have investigated the interaction of a single water or alcohol (methanol, ethanol, and 2-propanol) molecule with the exposed metal centers, namely, the Fe^{II}, Co^{II}, and Co^{III} active sites.

4.1.1 Fe^{II} active site. The calculated adsorption energies and metal–O distances for the interactions of water and the short-chain alcohols on the Fe^{II} site at the A-layer are summarized in Table 1.

At low coverages, water adsorbs in two distinct molecular conformations on top of the Fe^{II} site. The optimized structures, denoted as Mol-I and Mol-II, are presented in Fig. 2a and b, respectively. In both conformations, water forms two hydrogen bonds with the 3-fold coordinated oxygens from the lattice. The d_{OH-O} distances are similar, *i.e.* 1.73 and 1.70 Å for Mol-I and Mol-II, respectively. However, in the structure in Fig. 2a (Mol-I), the Fe site is significantly displaced from its initial position presented by a dark sphere. This rearrangement is reflected in the adsorption energy as well: Mol-I is by 16.5 kJ mol^{-1} less favorable than Mol-II. From the latter, a hydrogen atom can readily transfer to the surface with no apparent intermediate or barrier as indicated by the fact that the ZPVE-corrected energy at the saddle point of the electronic potential energy surface is energetically below that at the minimum for the molecularly adsorbed structure. The dissociated form of a single water molecule on top of Fe is shown in Fig. 2c. From the thermodynamic

Published on 08 September 2022. Downloaded on 10/6/2022 1:29:36 PM.

Table 1 Adsorption energies and metal–O distances for the interactions of water and short-chain alcohols on the Fe^{II} site at the (001)-A CFO surface

Adsorbate	State[a]	ΔE_{ads} [kJ mol^{-1}]	d_{Fe-O} [Å]	Figure[b]
Water	Mol-I	−124.2	2.08	Fig. 2a
	Mol-II	−145.7	2.06	Fig. 2b
	Diss	−145.9	1.91	Fig. 2c
	TS[c]	−148.0[e]	1.98	Fig. S3a
Methanol	Mol-I	−100.9	2.09	Fig. S1a
	Mol-II	−128.0	2.06	Fig. S1b
	Diss	−146.2	1.91	Fig. S1c
	TS[c]	−136.7[e]	1.99	Fig. S1d
Ethanol	Mol-I	−111.2	2.09	Fig. S2a
	Mol-II	−136.6	2.07	Fig. S2b
	Diss-I	−141.7	1.91	Fig. S2c
	Diss-II	−152.4	1.90	Fig. S2d
	TS[d]	−143.7[e]	2.00	Fig. S2e
2-Propanol	Mol-I	−113.0	2.11	Fig. 3a
	Mol-II	−143.0	2.07	Fig. 3b
	Diss-I	−151.6	1.92	Fig. 3c
	Diss-II	−159.3	1.91	Fig. 3d
	TS[d]	−149.9[e]	2.00	Fig. S3b

[a] Mol-molecular, Diss-dissociative, TS-transition state. [b] Figures starting with 'S' are given in ESI. [c] Transition state for: Mol-II → Diss. [d] Transition state for: Mol-II → Diss-I. [e] ZPVE-corrected energies at the TS on the electronic potential energy surface.

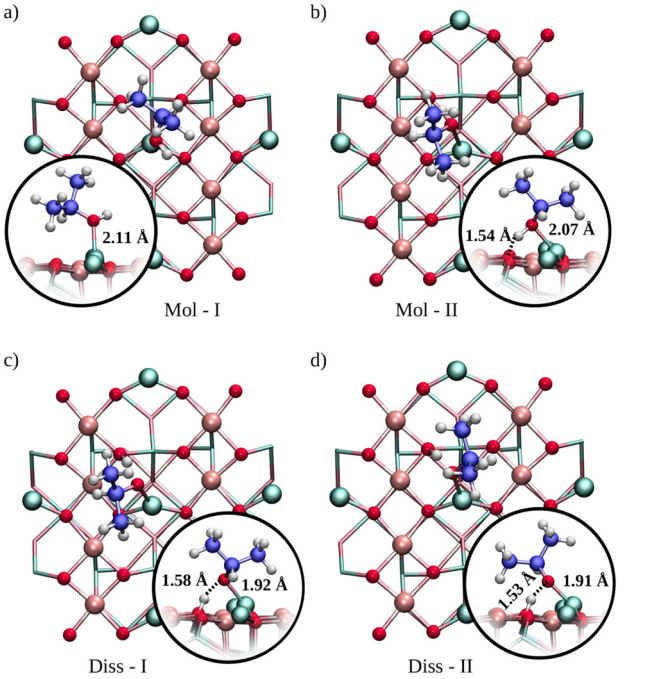


Fig. 3 Top and side views of the optimized geometries for the interactions of 2-propanol on the Fe^{II} active site at the (001)-A CFO surface: (a and b) molecular and (c and d) dissociated adsorption conformations. For the molecularly adsorbed 2-propanol, the abbreviations Mol-I and Mol-II are used to distinguish the conformations with an absence and a presence of a H-bond with the lattice oxygen, respectively. For the dissociatively adsorbed 2-propanol, the abbreviations Diss-I and Diss-II are used to distinguish two conformations with different orientations of the isopropyl group.

point of view, Mol-II and the dissociated conformation of water are predicted to coexist in equal amounts as indicated by the nearly identical adsorption energies of −145.7 and −145.9 kJ mol^{-1}, respectively.

Turning next to the adsorption of short-chain alcohols on top of the Fe^{II} site, once again, we distinguish two molecular adsorption conformations and a dissociated form involving O–H bond cleavage. For illustration, the optimized structures for 2-propanol are presented in Fig. 3.

The alcohol molecule binds to the Fe cation at the surface with its O atom. In the adsorption conformation characterized as Mol-I, there is no additional interaction of the alcohol with the surface as the alkyl part and the hydrogen atom from the OH functional group face upwards. By contrast, in the Mol-II structures the hydroxyl hydrogen points towards the 3-fold coordinated oxygen from the lattice forming H-bonds with lengths of 1.51, 1.53, and 1.54 Å for methanol, ethanol, and 2-propanol, respectively. Subsequent O–H dissociation and H-transfer to the lattice is facile, analogous to the water case, with no apparent activation energy. In the dissociated state,

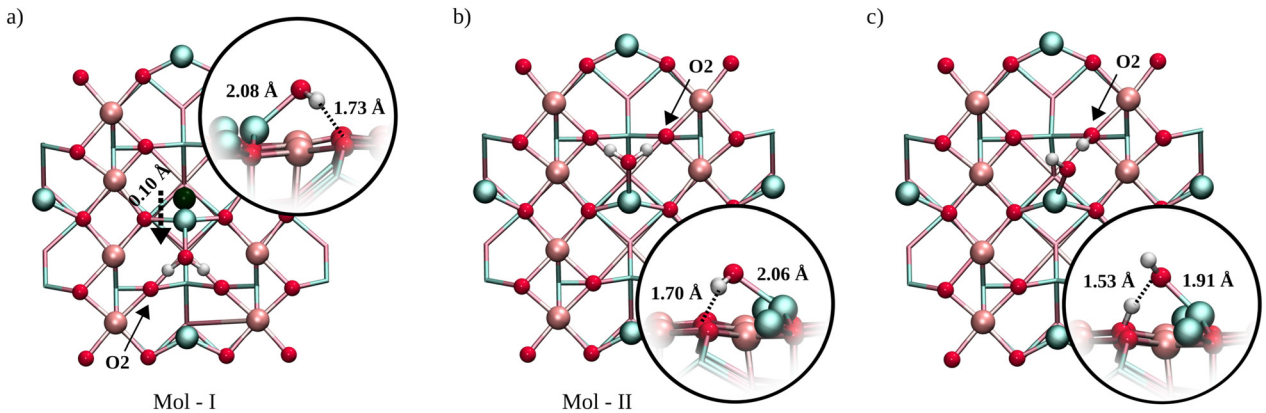


Fig. 2 Top and side views of the optimized geometries for the interactions of a single water molecule on the Fe^{II} active site at the (001)-A surface of CFO: (a and b) molecular and (c) dissociated adsorption conformations. The molecularly adsorbed water forms H-bonds with the 3-fold coordinated oxygens (O2) from the lattice, whereas in the dissociated case one of the hydrogens from water is transferred to this oxygen. The dark sphere represents the initial position of Fe before the adsorption.

 This journal is © the Owner Societies 2022

Published on 08 September 2022. Downloaded on 10/6/2022 1:29:36 PM.

the Fe–O interactions become stronger, with bond lengths that are by ~0.19 and 0.16 Å shorter in comparison to the Mol-I and Mol-II structures. The formed alkoxy species are stabilized by H-bonding, bridging the hosting Fe site and the surface OH. Furthermore, for ethanol and 2-propanol we find two distinct dissociated cases, namely Diss-I and Diss-II, based on the orientation of the alkyl group. The respective structures of these dissociated forms for 2-propanol are presented in Fig. 3c and d. The rotation of the isopropyl group from the Diss-I to the Diss-II case has to surpass an energy barrier of 12.4 kJ mol^{-1} before relaxing to a minimum which is by 7.7 kJ mol^{-1} more stable than the parent configuration.

By comparing the adsorption energies for the different adsorbate molecules and local minima in Table 1, one can notice that the energies, in general, become more negative in the following order: water > methanol > ethanol > 2-propanol. As a result, upon adsorption, alcohols should be able to replace hydroxyl groups from the surface. Regarding the different adsorption conformations, the Mol-II structure is always more favorable than Mol-I, and in its final state, the alcohol molecule is always found to deprotonate forming adsorbed alkoxy and surface hydroxyl groups, contrary to the water adsorption for which the molecular and dissociative states are competitive.

4.1.2 Co^{II} active site. Due to the strong relaxation pattern of the additional Fe cations at the A-layer, we distinguish two types of Co^{II} sites. These are the so-called 'free' and 'hindered' Co^{II} sites in Fig. 1b. The reactivity of the 'hindered' Co^{II} cations is compromised (to some extent) by the reduced bond lengths and the close proximity of the additional monolayer of Fe, whereas, as the names suggests, the 'free' Co^{II} remain more accessible as the Fe cations relax away.[24]

In the present study, we have considered the reactivity of both Co^{II} sites. The corresponding calculated adsorption energies and metal–O distances for the interactions of water and the short-chain alcohols are summarized in Table 2. In all cases, the interactions on the 'free' cobalt exhibit more negative adsorption energies.

On the other hand, the adsorption pattern of the adsorbates is identical for both sites. Water adsorbs only in a molecular fashion, bound additionally *via* a hydrogen bond to the 3-fold coordinated oxygen from the lattice, with d_{Co-O} = 2.11 (2.26) Å and d_{OH-O} = 1.62 (1.97) Å. The same holds true for the alcohol molecules, although in this case we observe two distinct molecular adsorptions: non-H-bonded (Mol-I) and H-bonded (Mol-II), just as for the Fe^{II} active site. In Mol-I, the alcohol molecule interacts with the surface only by binding to Co^{II}. On the 'free' cobalt, the d_{Co-O} distances are the same for the three alcohols with a value of 2.15 Å. On the 'hindered' cobalt these values are larger, *i.e.*, 2.21 Å for methanol and 2.22 Å for ethanol and 2-propanol. In Mol-II, the adsorbed alcohol coordinates to a cobalt cation such that the proton of the OH functional group orients towards a lattice oxygen forming a H-bond, with d_{OH-O} ranging from 1.64 to 1.72 (1.71 to 1.73) Å and d_{Co-O} of 2.12–2.13 (2.24) Å for the 'free' ('hindered') cobalt.

These findings show that the interactions on the 'hindered' Co^{II} are weaker, clearly reflecting the steric hindrance by the Fe monolayer. For both sites, Mol-II is energetically more stable, with adsorption energies that are by at least 16 kJ mol^{-1} more negative than for Mol-I (see Table 2).

4.1.3 Co^{III} active site. For the interactions of water and the short-chain alcohols on the Co^{III} active site at the B-layer of the CFO (001) surface, Table 3 summarizes the calculated adsorption energies and metal–O distances.

A single water molecule adsorbs molecularly on top of the Co^{III} site with d_{Co-O} = 1.92 Å. The dissociated case is by 66.5 kJ mol^{-1} less stable, and it is associated with a shorter d_{Co-O} of 1.77 Å.

Focusing on the energies for the alcohol adsorbates in Table 3, for methanol we observe different preference than for water; the dissociative adsorption prevails over the molecular one, although the energetic stability between the two cases differs by only 10.7 kJ mol^{-1}. For ethanol and 2-propanol, the molecular case is, once again, energetically more favored than the dissociative adsorption by 8.4 and 7.1 kJ mol^{-1}, respectively. In the dissociated state, the alkoxy species are stabilized by monodentate coordination on top of the hosting Co^{III} site such that the alcohol skeleton is inclined towards the surface ($\angle$ Co–O–C = 117.5° in methanol, 125.1° in ethanol, and 126.1° in 2-propanol).

A comparison of the adsorption energies reported in Tables 2 and 3, for the Co^{II} and Co^{III} sites, respectively, reveals that overall

Table 2 Adsorption energies and metal–O distances for the interactions of water and short-chain alcohols on the 'free' ('hindered') Co^{II} active site at the (001)-A CFO surface

Adsorbate	State[a]	ΔE_{ads} [kJ mol^{-1}]	d_{Co-O} [Å]	Figure[b]
Water	Mol	−95.9 (−78.0)	2.13 (2.26)	Fig. S4a (S5a)
Methanol	Mol-I	−77.2 (−63.4)	2.15 (2.21)	Fig. S4b (S5b)
	Mol-II	−98.0 (−80.0)	2.13 (2.24)	Fig. S4c (S5c)
Ethanol	Mol-I	−79.6 (−65.7)	2.15 (2.22)	Fig. S4d (S5d)
	Mol-II	−104.3 (−85.1)	2.12 (2.24)	Fig. S4e (S5e)
2-Propanol	Mol-I	−86.6 (−73.1)	2.15 (2.22)	Fig. S4f (S5f)
	Mol-II	−106.7 (−91.0)	2.12 (2.24)	Fig. S4g (S5g)

[a] Mol-molecular, Diss – dissociative. [b] Figures starting with 'S' are given in ESI.

Table 3 Adsorption energies and metal–O distances for the interactions of water and short-chain alcohols on the Co^{III} active site at the (001)-B CFO surface

Adsorbate	State[a]	ΔE_{ads} [kJ mol^{-1}]	d_{Co-O} [Å]	Figure[b]
Water	Mol	−94.0	1.92	Fig. S6a
	Diss	−27.5	1.77	Fig. S6b
	TS[c]	−27.7[d]	1.84	Fig. S6c
Methanol	Mol	−96.3	1.93	Fig. S7a
	Diss	−106.9	1.82	Fig. S7b
	TS[c]	−34.5[d]	1.85	Fig. S7c
Ethanol	Mol	−104.0	1.94	Fig. S8a
	Diss	−95.6	1.86	Fig. S8b
	TS[c]	−39.4[d]	1.86	Fig. S8c
2-Propanol	Mol	−108.4	1.94	Fig. S9a
	Diss	−101.4	1.86	Fig. S9b
	TS[c]	−39.2[d]	1.86	Fig. S9c

[a] Mol-molecular, Diss-dissociative, TS-transition state. [b] Figures starting with 'S' are given in ESI. [c] Transition state for: Mol → Diss. [d] ZPVE-corrected energies at the TS on the electronic potential energy surface.

Published on 08 September 2022. Downloaded on 10/6/2022 1:29:36 PM.

water and the short-chain alcohols bind more strongly to Co^{III}, with energies that differ by only a few kJ mol^{-1} for both oxidation states. The main difference in this comparison can be attributed to the adsorption mechanism, for which we observe no dissociation of the adsorbate on top of Co^{II}.

Finally, from the electronic structure perspective, the spin density on the Co^{III} site underneath the adsorbates is quenched (Fig. S11 of the ESI†), indicating that Co^{III} is in a low-spin configuration with all electrons paired. This result reflects earlier observations based on periodic DFT(PBE)+U calculations in a plane-wave basis, which showed that Co^{III} at the B-layer of CFO and Co_3O_4 prefers the low spin-state upon chemisorption of certain adsorbates.[13,24,26]

4.2 Adsorption at an oxygen vacancy

As for other spinels, the (001) CFO surfaces expose two types of oxygens: O1 and O2, marked in the cluster structures in Fig. 1. At both terminations (A and B), the O2 oxygen is 3-fold coordinated with two Co atoms from the surface and an inner Fe atom in tetrahedral position. Differently, the O1 oxygen is 3-fold coordinated at the B-layer (denoted as $O1^B$) with two Co atoms from the surface and an inner Fe atom in octahedral position. At the A termination, the O1 oxygen (denoted as $O1^A$) is 4-fold coordinated with an additional Fe from the surface layer.

To study the role of oxygen vacancies in the adsorption of water and short-chain alcohols, we removed a neutral O atom from the quantum cluster and limited our study to the most stable ones identified on the spinel (001) surfaces, *i.e.*, the $O1^B$ vacancy at the B-layer.[26,37] The adsorption energies for water, methanol, ethanol, and 2-propanol at the $O1^B$ vacancy are summarized in Table 4, together with the metal–O distances for the closest surface Co cations.

The interactions of the water/alcohol molecule with the vacancy follow a common adsorption pattern. Initially, the water/alcohol molecule adsorbs in a molecular fashion, forming a H-bond with another $O1^B$ lattice oxygen with d_{OH-O} distances in the 1.77–1.99 Å range. Next, the proton is transferred to the lattice oxygen. The dissociative adsorption at the $O1^B$ vacancy is by

Table 4 Adsorption energies and metal–O distances for the interactions of water and short-chain alcohols at the $O1^B$ vacancy on the (001)-B CFO surface

Adsorbate	State[a]	ΔE_{ads} [kJ mol^{-1}]	d_{Co-O} [Å]	Figure[b]
Water	Mol	−123.5	1.92/1.94	Fig. S12a
	Diss	−168.4	1.95/2.16	Fig. S12b
	TS[c]	−101.3[d]	2.53/2.95	Fig. S12c
Methanol	Mol	−127.5	2.63/2.63	Fig. S13a
	Diss	−165.2	1.96/2.14	Fig. S13b
	TS[c]	−89.9[d]	2.55/2.90	Fig. S13c
Ethanol	Mol	−132.3	2.53/2.69	Fig. S14a
	Diss	−175.1	1.96/2.14	Fig. S14b
	TS[c]	−93.6[d]	2.46/2.95	Fig. S14c
2-Propanol	Mol	−144.0	2.49/2.58	Fig. 4
	Diss	−168.7	1.95/2.14	Fig. 4
	TS[c]	−90.9[d]	2.51/2.61	Fig. 4

[a] Mol-molecular, Diss-dissociative, TS-transition state. [b] Figures starting with 'S' are given in ESI. [c] Transition state for: Mol → Diss. [d] ZPVE-corrected energies at the TS on the electronic potential energy surface.

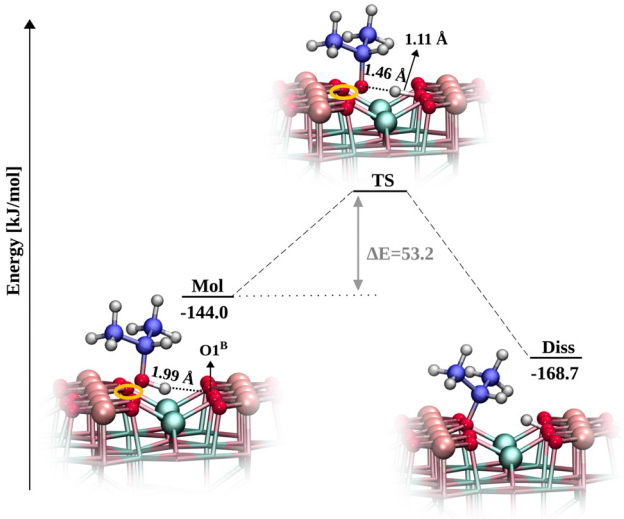


Fig. 4 Adsorption mechanism of a single 2-propanol molecule at the $O1^B$ vacancy of the (001)-B CFO surface. Initially, 2-propanol adsorbs in a molecular fashion (Mol) at the vacancy forming a H-bond with the oxygen from the lattice. After passing a transition state (TS) in which the H-proton is shifted mostly to the lattice oxygen, 2-propanol relaxes to the final geometry – the dissociative state (Diss).

24.7 to 44.9 kJ mol^{-1} more stable than molecular adsorption. A pictorial representation of the adsorption mechanism at the $O1^B$ vacancy is shown in Fig. 4 for 2-propanol. The cleavage of the O–H bond has the smallest energy cost for water, with a barrier of 22.2 kJ mol^{-1}. This barrier is largest for 2-propanol (53.1 kJ mol^{-1}), whereas for methanol and ethanol it is roughly isoenergetic (37.6 and 38.7 kJ mol^{-1}, respectively). In comparison to the O–H scission at the pristine surfaces, the activation energies at the oxygen vacancy are significantly higher than for the exothermic cases on the Fe^{II} site (Table 1), and smaller than those on the Co^{III} centers (~60 kJ mol^{-1}, see Table 3). On the other hand, the adsorption energies for the dissociated cases at the $O1^B$ vacancy are more negative than those on metal sites.

4.3 Infrared (IR) spectroscopy

To better understand the surface chemistry during the interactions of methanol, ethanol, and 2-propanol, on the (001) surfaces of CFO, the following sections compare results of *in situ* DRIFTS studies with simulated spectra from theory.

4.3.1 Methanol. The DRIFT spectra recorded at different pressures during the adsorption of methanol on CFO are plotted in Fig. 5.

First bands are visible already at pressures of 10^{-3} mbar; these include the spectroscopic dips at 3691 and 3635 cm^{-1}, and the adsorption bands at 2919, 2803, 1444, and 1068 cm^{-1}.

The negative bands are a direct consequence of the consumption of the OH groups from the hydroxylated CFO surfaces, suggesting dissociative adsorption of methanol. Accordingly, the signals at 2919 and 2803 cm^{-1}, can be assigned to the asymmetric and symmetric CH_3 stretching vibrations [$\nu_{as}(CH_3)$ and $\nu_s(CH_3)$], respectively, whereas the signals at 1444 and 1068 cm^{-1} can be assigned to the CH_3 bending [$\delta(CH_3)$], and

 This journal is © the Owner Societies 2022

Published on 08 September 2022. Downloaded on 10/6/2022 1:29:36 PM.

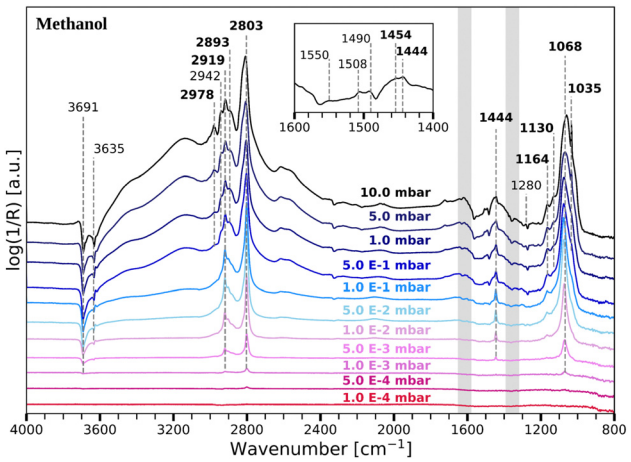


Fig. 5 The DRIFT spectra recorded at different pressures during the adsorption of methanol on the commercial CFO sample. The bands assigned to adsorbed methanol species are presented in bold to distinguish them from those corresponding solely to oxidation products. The very weak bands in the highlighted regions in grey indicate the presence of methyl formate and carbonates.

C–O stretching [ν(CO)] vibrations of methoxy species.[40–42] At slightly higher pressures of 10^{-2} mbar, a signal is also visible at 1164 cm^{-1}, accompanied by a shoulder at 1035 cm^{-1}. While these bands can be assigned to $\delta(CH_3)$ and ν(CO) of methoxy, respectively, they can be also indicative of molecularly adsorbed methanol.

Upon further increasing the pressure, the most prominent changes occur at 5×10^{-1} mbar, as summarized in the following. Several peaks centered at 2978, 2893 and 1454, 1130 become apparent and can be assigned to $\nu_{as}(CH_3)$, $\nu_s(CH_3)$, and $\delta(CH_3)$ of methanol adsorbed in a molecular fashion.[40,43] Some of these bands are superimposed and/or are at similar positions with those originating from oxidation products, the presence of which is further indicated by weak signals appearing in the regions between 1630–1580 cm^{-1} and 1320–1390 cm^{-1} (highlighted in grey in Fig. 5).[40–44] For instance, bands at 2942, 2893, 1600, 1587, 1454, 1380, and 1367 cm^{-1} may be attributed to the combination of ν_{as}(OCO) and δ(CH), ν(C–H), ν_{as}(OCO), δ(CH), and ν_s(OCO) of methyl formate species, whereas bands at 1490, 1380, and 1326 cm^{-1} may be attributed to monodentate carbonates.[40,41,43–45] For clarity, the vibrational frequencies which can be assigned to methoxy or molecularly adsorbed methanol are presented in bold in Fig. 5 to distinguish them from those corresponding solely to oxidation products. The broad signal formed in the region between 3500–3000 cm^{-1} infers the presence of physisorbed water as a side product from the adsorption of methanol on surface OH or the selective oxidation. On the other side, the broad feature in the region between 3000–2400 cm^{-1} may be indicative of the partial reduction of the spinel.[46] At 10 mbar, very weak bands at 1620, 1550, and 1280 cm^{-1} become visible suggesting the additional presence of bidentate carbonate species.[45]

To corroborate the assignment of the bands and species observed in the DRIFT spectra of methanol, in Table 5 we compare the experimental data (at 10 mbar) with calculated (and scaled) vibrational frequencies for the molecularly and dissociatively adsorbed methanol on the different active sites at the CFO (001) surfaces. The simulated IR intensities in the chemically significant regions are presented in Fig. 6. The vibrational assignments for the observed frequencies can be divided into three categories in terms of the characteristic modes of functional groups: CH_3 stretching in 3100–2700 cm^{-1}, CH_3 bending in 1500–1400 cm^{-1}, and C–O stretching and CH_3 wagging [$\omega(CH_3)$] in 1200–900 cm^{-1}.

Focusing first on the 3100–2700 cm^{-1} region and the CH_3 stretching vibrations, it is apparent that the $\nu_s(CH_3)$ modes, in general, display more intense signals than $\nu_{as}(CH_3)$, in accordance with the strong experimental peak of $\nu_s(CH_3)$ at 2803 cm^{-1} and the less intense $\nu_{as}(CH_3)$ peaks at 2978 and 2919 cm^{-1}. With the exception of the Diss state at the Co^{III} site, upon adsorption the calculated $\nu_s(CH_3)$ vibrations are displaced by 3 to 86 cm^{-1} to higher wave numbers relative to the frequency in isolated methanol.

Table 5 Calculated scaled vibrational frequencies of methanol and methoxide species in comparison with the experimental results from DRIFTS. All wave numbers are given in cm^{-1}. The following vibrational modes are listed: asymmetric and symmetric stretching and deformation modes of the methyl group [$\nu_{as}(CH_3)$, $\nu_s(CH_3)$ and $\delta_{as}(CH_3)$, $\delta_s(CH_3)$], wagging [$\omega(CH_3)$], and the CO stretching mode [ν(CO)]

Active site	State	$\nu_{as}(CH_3)$	$\nu_s(CH_3)$	$\delta_{as}(CH_3)$	$\delta_s(CH_3)$	$\omega(CH_3)$	ν(CO)
Fe^{II}	Mol-I	3052, 3035	2928	1466, 1456	1452	1097	983
	Mol-II	3024, 2987	2898	1453, 1450	1442	1165	1039
	Diss	2946, 2941	2864	1458, 1452	1441	1160	1053
'Free'-Co^{II}	Mol-I	3060, 2992	2906	1465, 1457	1427	1072	1019
	Mol-II	3029, 2983	2896	1472, 1455	1445	1153	1035
'Hindered'-Co^{II}	Mol-I	3044, 3006	2914	1480, 1447	1431	1071	1014
	Mol-II	3018, 2987	2900	1464, 1457	1444	1138	1030
Co^{III}	Mol	3083, 3052	2947	1465, 1441	1428	1103	984
	Diss	3029, 2846	2757	1419, 1334	1305	940	960
	Diss$_\perp$	2985, 2900	2801	1467, 1344	1304	954	1085
O1[b] vacancy	Mol	3024, 3019	2916	1473, 1425	1439	1119	979
	Diss	2980, 2953	2868	1475, 1461	1430	1159	1023
Free CH_3OH, calc.	—	3005, 2919	2861	1472, 1447	1452	1060	1054
Free CH_3OH, exp.[a]	—	3000, 2960	2844	1477, 1430[b]	1455	1060	1033
DRIFTS (at CFO), exp.	Mol & Diss	2978, 2919	2893, 2803	1454, 1444		1164, 1130	1068, 1035

[a] From ref. 38. [b] From ref. 39.

Published on 08 September 2022. Downloaded on 10/6/2022 1:29:36 PM.

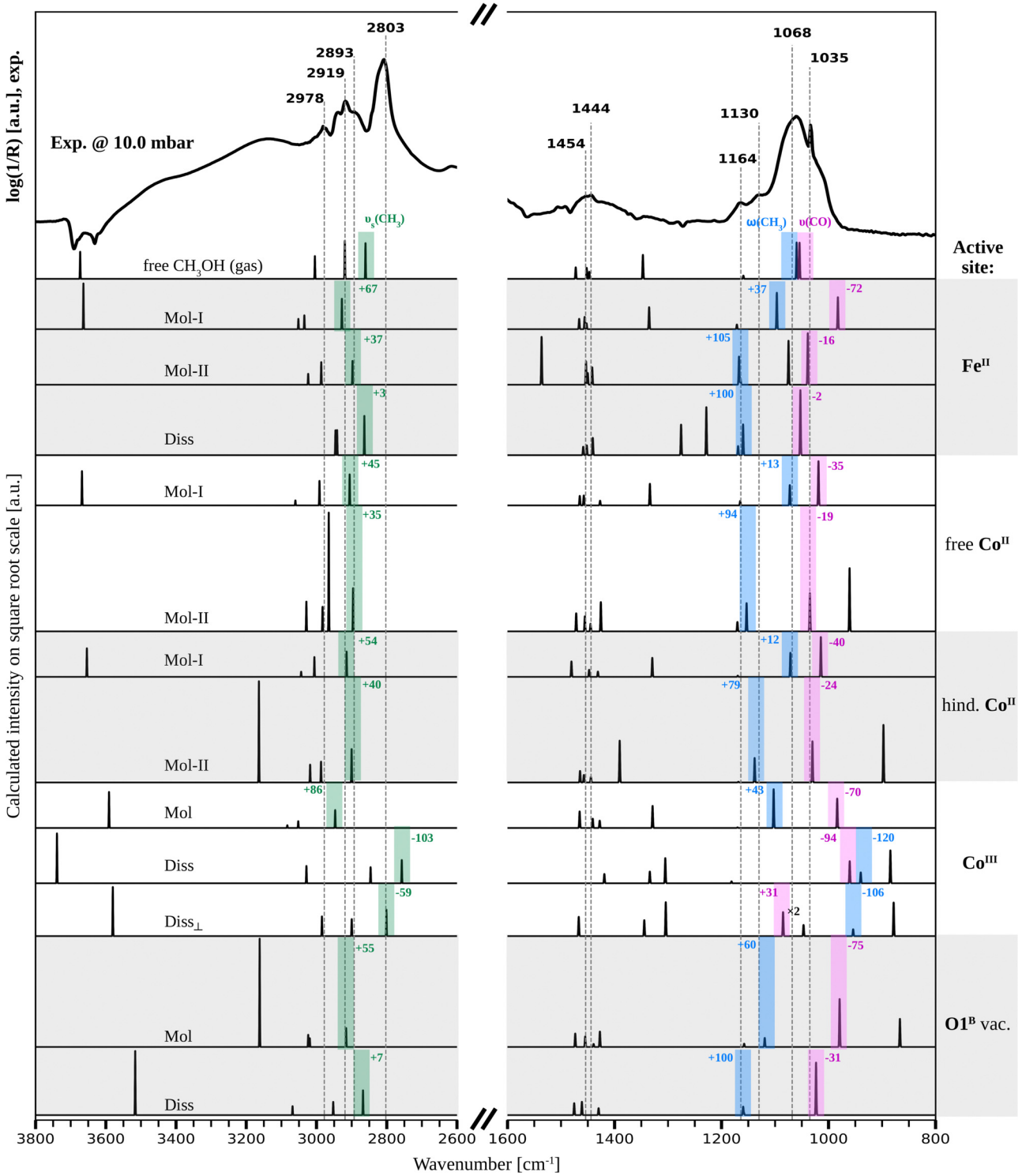


Fig. 6 A comparison of the experimental DRIFT spectra at 10.0 mbar with simulated IR spectra for the molecular and dissociative adsorptions of methanol on the different active sites at the CFO (001) surfaces.

Turning next to the 1500–1400 cm^{-1} region, a closer inspection of Table 5 shows that, for all equilibrium structures, the least affected modes by the adsorption on the surface are the deformations of the CH_3 group which, overall, are also weakest in intensity. The calculated frequencies of these modes agree rather well with those observed experimentally at 1444 and 1454 cm^{-1}. However, as they are positioned in close proximity to one another and with similar intensity, an exact and unambiguous assignment to individual experimental frequencies is not possible.

 This journal is © the Owner Societies 2022

Published on 08 September 2022. Downloaded on 10/6/2022 1:29:36 PM.

When we analyze the region between 1200 and 900 cm^{-1}, Fig. 6 shows strong to medium signals attributable to ν(CO) and $\omega(CH_3)$. Of these two modes, $\omega(CH_3)$ is almost always blue-shifted from 12 to 100 cm^{-1}, with the exception of the Diss geometry on Co^{III}, in which $\omega(CH_3)$ is red-shifted by 120 cm^{-1}. These findings corroborate the experimentally observed bands at 1164 and 1130 cm^{-1} (see Fig. 6). On the other hand, ν(CO) modes of adsorbed species are red-shifted by 2–94 cm^{-1} relative to free methanol. The frequency shifts associated with the ν(CO) vibrations strongly reflect the enlargement or diminution of the C–O bond length as a consequence of the different stabilization mechanisms of methanol on the surface sites. For instance, molecular adsorption conformations denoted as Mol-I on Fe^{II} and Mol on Co^{III} and the $O1^{B}$ vacancy are all associated with d_{C-O} = 1.43 Å, about 0.03 Å larger than in free methanol (1.40 Å) and, thus, exhibit major shifts of $\sim$80 cm^{-1} for ν(CO). On the other hand, Mol-I conformations on Co^{II} are associated with d_{C-O} = 1.42 Å and smaller shifts of $\sim$40 cm^{-1}. In the Mol-II adsorption structures, d_{C-O} = 1.41 Å and, consequently, the vibrational displacements are even smaller ($\sim$20 cm^{-1}). Regarding the dissociative adsorption, we recall from previous sections that, on Fe^{II}, methoxy is stabilized by H-bonding, such that it bridges the hosting Fe site and a lattice OH, while on Co^{III}, it is stabilized in a monodentate coordination on top of the metal center. As a result, the d_{C-O} bond length in the former is barely influenced (*i.e.*, it is the same as in free methanol, d_{C-O} = 1.40 Å) and the corresponding vibrational displacement is only 2 cm^{-1}, whereas in the latter, d_{C-O} is reduced by 0.04 Å (1.36 Å) and the ν(CO) mode is displaced by 94 cm^{-1}. While these observations support the experimental assignment that many ν(CO) bands of methoxy and molecularly adsorbed methanol may be superimposed at 1035 cm^{-1} and the broad feature on its right, they do not explain the very intense experimental peak at 1068 cm^{-1} attributable to ν(CO) of methoxy species and blue-shifted with respect to the isolated methanol molecule.

To explain the origin of the peak at 1068 cm^{-1}, we have focused on the Diss geometry at the pristine B-layer (*i.e.*, methoxy adsorption on top of the Co^{III} site) and additionally considered the dissociative adsorption of methanol with the C–O bond oriented perpendicular to the surface. For this structural configuration (hereafter denoted as $Diss_{\perp}$), we have fixed the initial positions of the O and C atoms of methoxy in two directions such that $\angle$ Co–O–C = 180° and allowed them to relax in the third direction along the surface normal. In the optimized $Diss_{\perp}$ geometry the resulting Co–O–C angle is 179.6°, the Co–O interaction weakens (d_{Co-O} = 1.96 Å), whereas the C–O bond strengthens (d_{C-O} = 1.35 Å) in comparison to Diss discussed so far and in which the alcohol skeleton is inclined toward the surface ($\angle$ Co–O–C = 117.5°, d_{Co-O} = 1.82 Å, d_{C-O} = 1.36 Å). The corresponding vibrational signature of $Diss_{\perp}$ is incorporated in Table 5 and Fig. 6. Noteworthy, the $\nu_{\perp}$(CO) mode is characterized by a positive shift of 31 cm^{-1} to higher wave numbers relative to the computed gas phase value and, thus, agrees rather well with the experimental signal at 1068 cm^{-1}, considering that this signal is by 35 cm^{-1} blue-shifted with respect to ν(CO) in free methanol (1033 cm^{-1}).

Analysis of the bonding motif of methoxy to Co^{III} using intrinsic bond orbitals (IBOs), for the Diss and $Diss_{\perp}$ structures, reveals seven occupied valence spin orbitals localized at the O moiety. One additional occupied spin orbital localized mainly at the Co has some contribution from an O 2p orbital, which for Diss is larger than for the $Diss_{\perp}$. These IBOs are collated in Fig. 7a and b, respectively. The interaction in Diss is coordinative in nature with a σ-donor lone pair on the O atom of methoxy and some π-back donation into a $2p_{\alpha}$ orbital of O. The final vibrational shift is a balance of these two synergistic bonding mechanisms which influence also the CO bond and the change in the effective mass for the vibrational mode. As a result, ν(CO) is red-shifted by 94 cm^{-1} in the tilted Diss structure. The reorientation from the tilted Diss to the perpendicular $Diss_{\perp}$ geometry is accompanied by a change of the hybridization at the O atom from sp^3-like to sp (cmp. Fig. 7b). The increased contribution from the O 2s orbital to the CO bond strengthens the latter (as it is apparent from the shortened bond length) and blue shifts $\nu_{\perp}$(CO). Consequently, we reason that the positive ν(CO) vibrational shift observed in the DRIFT spectrum arises from the change in hybridization

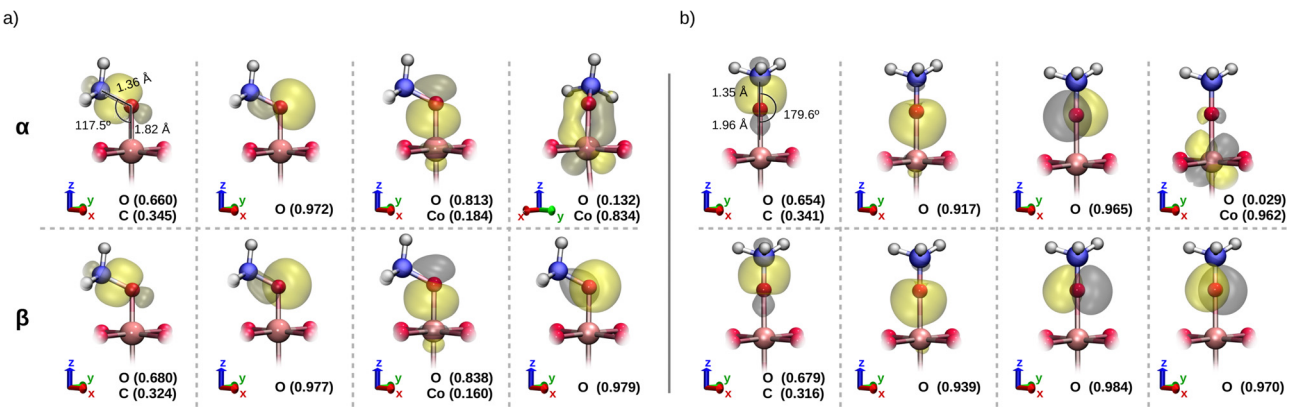


Fig. 7 Singly occupied IBOs localized at the O atom of methoxy in the (a) Diss and (b) $Diss_{\perp}$ geometries on the Co^{III} site at the B-layer. Isosurface value is ±0.05.

Published on 08 September 2022. Downloaded on 10/6/2022 1:29:36 PM.

when the methoxy group is forced into a perpendicular geometry by neighbouring hydroxy or methoxy groups on the surface, at high coverage.

Another interesting observation from this analysis is that, upon dissociation of methanol, the hosting Co^{III} site holds on to its original $3d^6$ state. Instead, the neighboring Co acts as an actual electron acceptor center and is reduced to the divalent state, as can be inferred by seven IBOs localized at this atom, with occupation numbers ≈ 1 and consisting mainly of its 3d orbitals. The same conclusion can be reached from the IBO analysis for the analogous dissociated cases of ethanol and 2-propanol on top of Co^{III}.

4.3.2 Ethanol and 2-propanol. The DRIFT spectra recorded at different pressures during the adsorption of ethanol and 2-propanol on CFO are presented in Fig. 8 and 9, respectively.

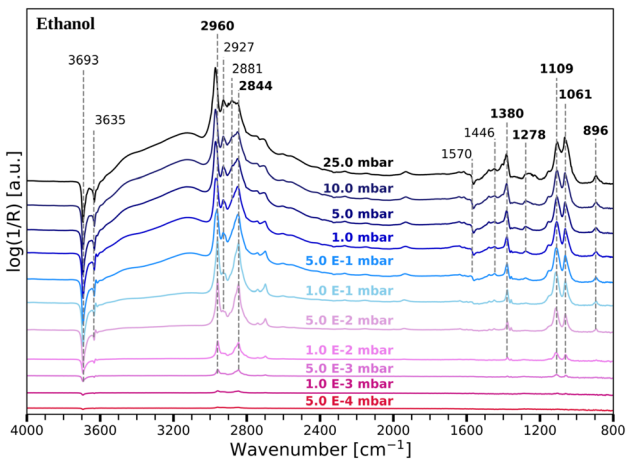


Fig. 8 The DRIFT spectra recorded at different pressures during the adsorption of ethanol on the commercial CFO sample. The bands assigned to adsorbed ethanol species are presented in bold to distinguish them from those corresponding solely to oxidation products.

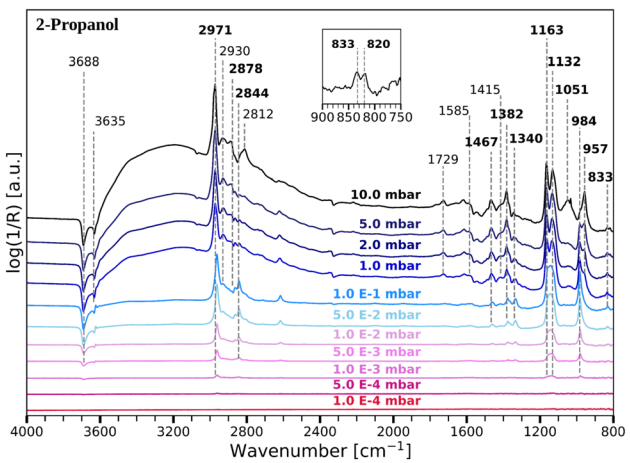


Fig. 9 The DRIFT spectra recorded at different pressures during the adsorption of 2-propanol on the commercial CFO sample. The bands assigned to adsorbed 2-propanol species are presented in bold to distinguish them from those corresponding solely to oxidation products.

Focusing first on the vibrational signature of ethanol in Fig. 8, first bands are visible at 5×10^{-3} mbar and centered at 2960, 2844, 1380, and 1109, 1061 cm^{-1}. They can be assigned to $\nu_{as}(CH_3)$, $\nu_{as}(CH_2)$, $\delta(CH_3)$, and coupled $\nu(CC)/\nu(CO)$ stretching modes of ethoxide.[46–48] In parallel, the spectroscopic dips at 3693 and 3635 cm^{-1} suggest dissociation of ethanol by condensation with surface OH, similar to what was observed for methanol. Above 5×10^{-2} mbar broadening of the formerly observed bands as well as the detection of bands at 1278 and 896 cm^{-1} which can be assigned to $\delta(OH)$ and $\nu_s(CCO)$ indicate the presence of molecularly adsorbed ethanol.[46,48,49] In addition, at higher pressures the 2960 cm^{-1} band is blue-shifted, peaking at 2972 cm^{-1} at 25.0 mbar. A weak band at 1635 cm^{-1} suggests the formation of acetaldehyde.[46,48] Acetaldehyde is then further oxidized forming acetate which is detected by bands at 1570, 1446, and 1335 cm^{-1} assigned to $\nu_{as}(OCO)$, $\nu_s(OCO)$, and $\delta(CH_3)$. Oxidation is evidenced by a broad adsorption feature in the $\nu(OH)$ region between 3600–3000 cm^{-1} indicating the presence of physisorbed water above 5×10^{-1} mbar. Similar to methanol adsorption, partial reduction of the spinel is suggested by a broad feature in the region between 3000–2400 cm^{-1}.[46] Furthermore, the presence of carbonates is indicated at pressures above 5 mbar.

Turning next to 2-propanol and its vibrational signature in Fig. 9, the first signals are also visible at 5×10^{-3} mbar. The bands at 2971, 2844, 1382, 1340, and 1132, 984 cm^{-1} can be assigned to $\nu_{as}(CH_3)$, $\nu(CH)$, $\delta_{as}(CH_3)$, $\delta_s(CH_3)$, and coupled $\nu(CC)/\nu(CO)$ mixed with CH_3 rocking $[\rho(CH_3)]$.[15,46,50–55] Likewise to the adsorption of methanol and ethanol, 2-propoxide is formed by condensation of 2-propanol with surface OH as suggested by negative bands at 3688 and 3635 cm^{-1}. Broadening of the bands at 1×10^{-1} mbar gives rise to peaks at 2878, 1163, 1051, 957, and 833, 820 cm^{-1} which can be assigned to $\nu(CH)$, $\nu(CC)$ and $\omega(CH_3)$ association, $\nu(CO)$, $\rho(CH_3)$, and $\nu(CC)$ of molecularly adsorbed or gas-phase 2-propanol.[56] At 1 mbar bands at 1729, 1585, 1415, 1336 cm^{-1} emerge together with a broad absorption between 3600–3000 cm^{-1} which indicates the oxidation of 2-propanol forming acetate, acetone, and water. The band at 1729 cm^{-1} is assigned to $\nu(C{=}O)$ of acetone and bands at 1585, 1415, 1336 cm^{-1} are ascribed to $\nu_{as}(OCO)$, $\nu_s(OCO)$, and $\delta(CH_3)$ of acetate.[15,54,57–60]

A comparison of the experimental frequencies with the calculated ones for the different interactions of ethanol and 2-propanol on the (001) CFO surfaces is presented in Tables 6 and 7, respectively, whereas the corresponding simulated IR intensities are shown in Fig. S15 and S16 of ESI.†

In the C–H stretch region from 3100 to 2800 cm^{-1}, the bands corresponding to $\nu(CH_2)$ in ethanol and $\nu(CH)$ in 2-propanol undergo the most pronounced shifts. For instance, $\nu_{as}(CH_2)$ modes in the adsorbed ethanol molecules suffer significant shifts of $\sim$26 to 118 cm^{-1} whereas the $\nu_{as}(CH_3)$ modes are displaced by $\sim$2 to 45 cm^{-1}. On the other hand, the $\nu(CH)$ bands in the adsorbed 2-propanol molecules experience shifts of $\sim$3 to 98 cm^{-1} whereas $\nu_{as}(CH_3)$ bands are shifted by $\sim$2 to 53 cm^{-1}. These frequency shifts are, in part, related to the enlargement or diminution of the C–O bond in the adsorbed

 This journal is © the Owner Societies 2022

Published on 08 September 2022. Downloaded on 10/6/2022 1:29:36 PM.

Table 6 Calculated scaled vibrational frequencies of ethanol and ethoxide species in comparison with the experimental results from DRIFTS. All wave numbers are given in cm^{-1}. The following vibrational modes are listed: asymmetric stretching of the CH_3 and CH_2 groups [$\nu_{as}(CH_3)$ and $\nu_{as}(CH_2)$], symmetric bending of CH_3 [$\delta_s(CH_3)$], bending of OH [δ(OH)], coupled CO and CC stretching [ν(CO)/ν(CC)], and the CCO symmetric stretching [ν(CCO)]

Active site	State	$\nu_{as}(CH_3)$	$\nu_{as}(CH_2)$	$\delta_s(CH_3)$	δ(OH)	ν(CO)/ν(CC)	ν_s(CCO)
Fe^{II}	Mol-I	3034, 3019	3005	1374	1260	1094, 1037	864
	Mol-II	3029, 2998	2961	1353	—	1090, 1071	880
	Diss	3015, 2994	2913	1346	—	1098, 1057	884
'Free'-Co^{II}	Mol-I	3033, 3008	3029	1365	1251	1069, 1037	875
	Mol-II	3029, 3027	2947	1370	—	1091, 1060	878
'Hindered'-Co^{II}	Mol-I	3032, 3017	3000	1363	1244	1068, 1034	871
	Mol-II	3038, 3005	2952	1359	—	1091, 1047	895
Co^{III}	Mol	3051, 3035	2993	1359	1264	1050, 1037	873
	Diss	3072, 3053	2980	1332	—	1043, 902	877
	$Diss_{\perp}$	3045, 3034	2836	1387	—	1066, 1026	888
$O1^{B}$ vacancy	Mol	3021, 3008	2898	1366	—	1053, 1032	855
	Diss	3029, 3009	2941	1384	—	1071, 1056	885
Free CH_3CH_2 OH, calc.	—	3027, 3024	2886	1357	1252	1110, 1037	885
Free CH_3CH_2 OH, exp.[a]	—	2992, 2987	2901	1367	1241	1090, 1027	885[b]
DRIFTS (at CFO), exp.	Mol & Diss	2960 (2972)	2844	1380	1278	1109, 1061	896

[a] From ref. 61. [b] From ref. 49.

Table 7 Calculated scaled vibrational frequencies of 2-propanol and 2-propoxide species in comparison with the experimental results from DRIFTS. All wave numbers are given in cm^{-1}. The following vibrational modes are listed: asymmetric stretching of CH_3 [$\nu_{as}(CH_3)$], CH stretching [ν(CH)], symmetric bending of CH_3 [$\delta_s(CH_3)$], coupled CO and CC stretching with CH_3 rocking [ν(CO)/ν(CC)/$\rho(CH_3)$], and the CC stretching [ν(CC)]

Active site	State	$\nu_{as}(CH_3)$[a]	ν(CH)	$\delta_s(CH_3)$	ν(CO)/ν(CC)/$\rho(CH_3)$			ν(CC)
Fe^{II}	Mol-I	3013, 3011	2944	1412, 1387	1179	1133	965	819
	Mol-II	3029, 2991	2864	1385, 1379	1176	1141	973	832
	Diss	3020, 3016	2844	1375, 1373	1165	1150	1006	845
'Free'-Co^{II}	Mol-I	3028, 3009	2908	1399, 1373	1177	1154	975	826
	Mol-II	3030, 3021	2907	1376, 1358	1163	1133	988	826
'Hindered'-Co^{II}	Mol-I	3015, 3010	2908	1373, 1354	1190	1146	972	824
	Mol-II	3014, 3002	2899	1373, 1350	1191	1159	984	842
Co^{III}	Mol	3040, 3018	2922	1383, 1352	1178	1126	959	828
	Diss	3048, 3041	2891	1365, 1335	1126	1060	938	815
	$Diss_{\perp}$	3067, 3053	2883	1369, 1356	1122	1069	893	813
$O1^{B}$ vacancy	Mol	3021, 2994	2945	1367, 1337	1163	1135	947	803
	Diss	3012, 2997	2895	1390, 1377	1142	1106	948	819
Free $(CH_3)_2$ CHOH, calc.	—	3023, 3000	2847	1378, 1360	1187	1155	981	829
Free $(CH_3)_2$ CHOH, exp.[b]	—	2979, 2971	2884	1391, 1381	1153	1130	—	830[c]
DRIFTS (at CFO), exp.	Mol & Diss	2971	2878, 2844	1340	1163, 1132, 1051, 984, 957			833, 820

[a] Frequencies of the two most intense peaks. [b] From ref. 62. [c] From ref. 56.

species (up to 0.05 Å for both alcohols). Similarly as for methanol, the deformation modes of the CH_3 and CH_2 functional groups are located in close proximity to one another in the region between 1500 and 1280 cm^{-1} and experience only minor to moderate shifts.

Analysis of the calculated spectra of ethanol and 2-propanol in comparison to the experimental ones in the region between 1200 and 900 cm^{-1}, characteristic for the ν(CO) vibration, is a tentative task since many motions are coupled and/or in close proximity to one another, hampering an exact assignment to individual frequencies and modes. In adsorbed ethanol, the ν(CO) mode is coupled to ν(CC). We, thus, scale the vibrations which are heavily dominated by the collective C–C–O motions with a value obtained by averaging over the scaling factors for ν(CO), ν(CC), and ν_s(CCO) of gas phase ethanol (*i.e.*, 0.956). Experimentally, the collective ν(CO)/ν(CC) motions of ethoxide and molecularly adsorbed ethanol at 1109 and 1061 cm^{-1} peak 48 cm^{-1} apart. This frequency difference between the two bands is particularly similar to that calculated for Diss on Fe^{II} (41 cm^{-1}) and $Diss_{\perp}$ on Co^{III} (40 cm^{-1}, here, as for methanol, C–O is oriented perpendicular to the surface – Fig. S10a of the ESI†). From the molecular adsorption configurations, this value is close to that calculated for Mol-II on the hindered Co^{II} site (44 cm^{-1}). For 2-propanol, the ν(CO)/ν(CC) vibrations are additionally coupled to $\rho(CH_3)$. We can identify all the assignments obtained experimentally for the collective ν(CO)/ν(CC)/$\rho(CH_3)$ motions; in general, for all interactions, two such bands are predicted in the region above 1100 cm^{-1} whereas a third band is expected below 1000 cm^{-1}.

For ethanol, the calculated frequencies for the OH bending and the symmetric C–C–O stretching modes, which are shifted by 0–13 cm^{-1} and 1–21 cm^{-1} with respect to the values in gas phase (see Table 6), support the assignment of the experimental bands at 1278 and 896 cm^{-1}. The same holds true for

Published on 08 September 2022. Downloaded on 10/6/2022 1:29:36 PM.

the ν(CC) vibration in adsorbed 2-propanol, displaced by up to 25 cm^{-1} and expected in the proximity of the experimental bands at 833 and 820 cm^{-1}.

Overall, the trends predicted by the DFT calculations for the characteristic bands of ethanol and 2-propanol are in a good qualitative agreement with the ones observed in the DRIFT spectra. We note, however, that the commercial sample of CFO exposes facets of different crystallographic orientations and the CFO surfaces are associated with higher adsorption coverage under experimental conditions. These factors can have an impact on the frequency shifts of the vibrational modes, either indirectly, by introducing electronic and magnetic structure changes in the surface (thereof influencing the bonding properties of the active sites), or directly, through adsorbate–adsorbate vibrational coupling.[63,64]

5 Conclusions

Spinel oxides containing earth-abundant metals such as Co and Fe have gained an increasing attention in recent years due to their affordable cost and catalytic performance in the oxidation of organics, in particular, for the selective oxidation of alcohols. Using embedded cluster models, we investigated the adsorption mechanism of water and the short-chain alcohols: methanol, ethanol, and 2-propanol, on the Co-terminated (001) surfaces of spinel CFO, as a basic phenomenon of the catalytic redox cycles. We considered the Fe^{II} and Co^{II} metal centers as active sites at the A termination and Co^{III} at the B termination.

On top of Fe^{II}, the adsorbates dissociate with no apparent intermediate or barrier. By contrast, on the Co^{II} sites, the alcohols adsorb in a molecular fashion in two distinct geometries: H-bonded and non-H-bonded to lattice oxygen. The H-bonded structures are predicted to be more stable than the non-H-bonded adsorption conformations. A comparison of the interactions on Co^{II} and Co^{III} shows that the absorbates bind more strongly to the latter, on which the dissociative state is also observed.

Water and the alcohol molecules can also adsorb at oxygen vacancies. In fact, the O1 vacancy at the B-layer shows the strongest affinity toward these adsorbates relative to the adsorption on metal sites at pristine surfaces. In the final state, the adsorbates dissociate at the vacancy, lifting the reconstructions introduced by the defect and resulting in partially hydroxylated surfaces. The activation energies for the dissociation are larger than the exothermic cases on Fe^{II} and smaller than those on Co^{III}.

In general, the interactions of the alcohols with the CFO (001) surfaces are associated with more negative adsorption energies than those of water, implying that alcohols are able to replace OH groups from the surface. This observation is further validated by the DRIFTS experiments, which revealed that methanol, ethanol, and 2-propanol, adsorb mainly dissociatively on the commercial CFO sample by a condensation with surface OH. With increasing the pressure, adsorption of molecular alcohol species is also evidenced. By combining the available experimental information from DRIFTS with the simulated IR spectra for methanol on the (001) surfaces of CFO, an interesting inference can be pointed out: a strong spectroscopic signal of a blue-shifted ν(CO) at 1068 cm^{-1} can be interpreted in terms of oriental changes of the alcohol skeleton with preferential orientation perpendicular to the surface after adsorption. The corresponding frequency shift is then related to the change of the hybridization at the O atom of methoxy from sp^3-like to sp, going from the tilted to the perpendicular geometry. For ethanol and 2-propanol, the structurally sensitive ν(CO) mode vibrates collectively with ν(CC) and $\rho(CH_3)$ in the region below 1200 cm^{-1}, hampering an independent assignment. Overall, the simulated IR data is in a good qualitative agreement with the bands observed in the DRIFTS experiments.

Conflicts of interest

There are no conflicts to declare.

Acknowledgements

This project was funded by the Deutsche Forschungsgemeinschaft (DFG, German Research Foundation) – 388390466 – TRR 247 (Project A1 and A5). The work has been supported by the ''Center for Solvation Science ZEMOS'' funded by the German Federal Ministry of Education and Research BMBF and by the Ministry of Culture and Research of Nord Rhine-Westphalia.

Notes and references

1 Q. Zhao, Z. Yan, C. Chen and J. Chen, *Chem. Rev.*, 2017, **117**, 10121–10211.
2 P. Bothra and S. K. Pati, *ACS Energy Lett.*, 2016, **1**, 858–862.
3 K. Chakrapani, G. Bendt, H. Hajiyani, I. Schwarzrock, T. Lunkenbein, S. Salamon, J. Landers, H. Wende, R. Schlögl and R. Pentcheva, *et al.*, *ChemCatChem*, 2017, **9**, 2988–2995.
4 D. Gu, C.-J. Jia, C. Weidenthaler, H.-J. Bongard, B. Spliethoff, W. Schmidt and F. Schüth, *J. Am. Chem. Soc.*, 2015, **137**, 11407–11418.
5 T. Baidya, T. Murayama, P. Bera, O. V. Safonova, P. Steiger, N. K. Katiyar, K. Biswas and M. Haruta, *J. Phys. Chem. C*, 2017, **121**, 15256–15265.
6 Z.-Y. Tian, P. Mountapmbeme Kouotou, A. El Kasmi, P. H. Tchoua Ngamou, K. Kohse-Höinghaus, H. Vieker, A. Beyer and A. Gölzhäuser, *Proc. Combust. Inst.*, 2015, **35**, 2207–2214.
7 Y. Hammiche-Bellal, A. Benadda, L. Meddour-Boukhobza, S. Barama, A. Djadoun and A. Barama, *Catal. Commun.*, 2013, **42**, 62–67.

 This journal is © the Owner Societies 2022

Published on 08 September 2022. Downloaded on 10/6/2022 1:29:36 PM.

8 M. Hähsler, J. Landers, T. Nowack, S. Salamon, M. Zimmermann, S. Heißler, H. Wende and S. Behrens, *Inorg. Chem.*, 2020, **59**, 3677–3685.
9 D. Fritsch and C. Ederer, *Phys. Rev. B: Condens. Matter Mater. Phys.*, 2010, **82**, 104117.
10 D. Fritsch and C. Ederer, *Phys. Rev. B: Condens. Matter Mater. Phys.*, 2012, **86**, 014406.
11 F. Cavani, N. Ballarini and A. Cericola, *Catal. Today*, 2007, **127**, 113–131.
12 T. Bürgi and M. Bieri, *J. Phys. Chem. B*, 2004, **108**, 13364–13369.
13 S. Anke, G. Bendt, I. Sinev, H. Hajiyani, H. Antoni, I. Zegkinoglou, H. Jeon, R. Pentcheva, B. Roldan Cuenya and S. Schulz, *et al.*, *ACS Catal.*, 2019, **9**, 5974–5985.
14 T. Falk, E. Budiyanto, M. Dreyer, C. Pflieger, D. Waffel, J. Büker, C. Weidenthaler, K. F. Ortega, M. Behrens and H. Tüysüz, *et al.*, *ChemCatChem*, 2021, **13**, 2942–2951.
15 S. Anke, T. Falk, G. Bendt, I. Sinev, M. Hävecker, H. Antoni, I. Zegkinoglou, H. Jeon, A. Knop-Gericke and R. Schlögl, *et al.*, *J. Catal.*, 2020, **382**, 57–68.
16 K. Friedel Ortega, S. Anke, S. Salamon, F. Özcan, J. Heese, C. Andronescu, J. Landers, H. Wende, W. Schuhmann and M. Muhler, *et al.*, *Chem. – Eur. J.*, 2017, **23**, 12443–12449.
17 S. Najafishirtari, K. F. Ortega, M. Douthwaite, S. Pattisson, G. J. Hutchings, C. J. Bondue, K. Tschulik, D. Waffel, B. Peng and M. Deitermann, *et al.*, *Chem. – Eur. J.*, 2021, **27**, 16809–16833.
18 C.-Q. Lv, C. Liu and G.-C. Wang, *Catal. Commun.*, 2014, **45**, 83–90.
19 D. Mei, N. A. Deskins, M. Dupuis and Q. Ge, *J. Phys. Chem. C*, 2008, **112**, 4257–4266.
20 T. Watanabe, M. Ehara, K. Kuramoto and H. Nakatsuji, *Surf. Sci.*, 2009, **603**, 641–646.
21 M. Mavrikakis and M. A. Barteau, *J. Mol. Catal. A: Chem.*, 1998, **131**, 135–147.
22 M. Calatayud, A. Markovits, M. Menetrey, B. Mguig and C. Minot, *Catal. Today*, 2003, **85**, 125–143.
23 A. Rushiti and C. Hättig, *Chem. – Eur. J.*, 2021, **27**, 17115–17126.
24 H. Hajiyani and R. Pentcheva, *ACS Catal.*, 2018, **8**, 11773–11782.
25 X. Shi, S. L. Bernasek and A. Selloni, *J. Phys. Chem. C*, 2016, **120**, 14892–14898.
26 A. Rushiti, C. Hättig, B. Wen and A. Selloni, *J. Phys. Chem. C*, 2021, **125**, 9774–9781.
27 A. M. Burow, M. Sierka, J. Döbler and J. Sauer, *J. Chem. Phys.*, 2009, **130**, 174710.
28 TURBOMOLE V7.4, 2019, a development of University of Karlsruhe and Forschungszentrum Karlsruhe GmbH, 1989–2007, TURBOMOLE GmbH, since 2007, available from **https://www.turbomole.com**.
29 C. Adamo and V. Barone, *J. Chem. Phys.*, 1999, **110**, 6158–6170.
30 F. Weigend and R. Ahlrichs, *Phys. Chem. Chem. Phys.*, 2005, **7**, 3297–3305.
31 A. M. Burow, M. Sierka and F. Mohamed, *J. Chem. Phys.*, 2009, **131**, 214101.
32 G. Igel-Mann, *PhD Thesis*, Stuttgart, 1987.
33 G. Igel-Mann, H. Stoll and H. Preuss, *Mol. Phys.*, 1988, **65**, 1321–1328.
34 P. Plessow, *J. Chem. Theory Comput.*, 2013, **9**, 1305–1310.
35 T. Helgaker, *Chem. Phys. Lett.*, 1991, **182**, 503–510.
36 S. Høst, J. Olsen, B. Jansk, L. Thøgersen, P. Jørgensen and T. Helgaker, *J. Chem. Phys.*, 2008, **129**, 124106.
37 X. Shi, S. L. Bernasek and A. Selloni, *J. Phys. Chem. C*, 2017, **121**, 3929–3937.
38 T. Shimanouchi, *Tables of Molecular Vibrational Frequencies Part 1.*, National Bureau of Standards, Washington, DC, 1967.
39 H. D. Noether, *J. Chem. Phys.*, 1942, **10**, 693–699.
40 J. Koßmann, G. Roßmüller and C. Hättig, *J. Chem. Phys.*, 2012, **136**, 034706.
41 K. Kähler, M. C. Holz, M. Rohe, A. C. van Veen and M. Muhler, *J. Catal.*, 2013, **299**, 162–170.
42 M. M. Natile and A. Glisenti, *Chem. Mater.*, 2002, **14**, 3090–3099.
43 G. Busca and V. Lorenzelli, *J. Catal.*, 1980, **66**, 155–161.
44 V. Crocella, F. Cavani, G. Cerrato, S. Cocchi, M. Comito, G. Magnacca and C. Morterra, *J. Phys. Chem. C*, 2012, **116**, 14998–15009.
45 L. Lukashuk, N. Yigit, R. Rameshan, E. Kolar, D. Teschner, M. Hävecker, A. Knop-Gericke, R. Schlögl, K. Föttinger and G. Rupprechter, *ACS Catal.*, 2018, **8**, 8630–8641.
46 J. V. Ochoa, C. Trevisanut, J.-M. M. Millet, G. Busca and F. Cavani, *J. Phys. Chem. C*, 2013, **117**, 23908–23918.
47 W.-C. Wu, C.-C. Chuang and J.-L. Lin, *J. Phys. Chem. B*, 2000, **104**, 8719–8724.
48 O. Vozniuk, S. Agnoli, L. Artiglia, A. Vassoi, N. Tanchoux, F. Di Renzo, G. Granozzi and F. Cavani, *Green Chem.*, 2016, **18**, 1038–1050.
49 A. Barnes and H. Hallam, *Trans. Faraday Soc.*, 1970, **66**, 1932–1940.
50 G. Busca, E. Finocchio, V. Lorenzelli, G. Ramis and M. Baldi, *Catal. Today*, 1999, **49**, 453–465.
51 X. Wang, Y. Liu, T. Zhang, Y. Luo, Z. Lan, K. Zhang, J. Zuo, L. Jiang and R. Wang, *ACS Catal.*, 2017, **7**, 1626–1636.
52 G. S. Foo, F. Polo-Garzon, V. Fung, D.-E. Jiang, S. H. Overbury and Z. Wu, *ACS Catal.*, 2017, **7**, 4423–4434.
53 Q. Gu, X. Fu, X. Wang, S. Chen, D. Y. Leung and X. Xie, *Appl. Catal., B*, 2011, **106**, 689–696.
54 T. Bürgi and M. Bieri, *J. Phys. Chem. B*, 2004, **108**, 13364–13369.
55 M. Dreyer, D. Cruz, U. Hagemann, P. Zeller, M. Heidelmann, S. Salamon, J. Landers, A. Rabe, K. F. Ortega and S. Najafishirtari, *et al.*, *Chem. – Eur. J.*, 2021, **27**, 17127–17144.
56 J. Green, *Trans. Faraday Soc.*, 1963, **59**, 1559–1563.
57 F. Arsac, D. Bianchi, J. Chovelon, C. Ferronato and J. Herrmann, *J. Phys. Chem. A*, 2006, **110**, 4202–4212.
58 M. El-Maazawi, A. Finken, A. Nair and V. Grassian, *J. Catal.*, 2000, **191**, 138–146.

59 N. Fouad, P. Thomasson and H. Knözinger, *Appl. Catal., A*, 2000, **196**, 125–133.
60 Q. Ren, S. Mo, R. Peng, Z. Feng, M. Zhang, L. Chen, M. Fu, J. Wu and D. Ye, *J. Mater. Chem. A*, 2018, **6**, 498–509.
61 J. R. Durig, H. Deeb, I. D. Darkhalil, J. J. Klaassen, T. K. Gounev and A. Ganguly, *J. Mol. Struc.*, 2011, **985**, 202–210.
62 S. A. Fuente, C. A. Ferretti, N. F. Domancich, V. K. Dez, C. R. Apestegua, J. I. Di Cosimo, R. M. Ferullo and N. J. Castellani, *Appl. Surf. Sci.*, 2015, **327**, 268–276.
63 R. Linke, D. Curulla, M. Hopstaken and J. Niemantsverdriet, *J. Chem. Phys.*, 2001, **115**, 8209–8216.
64 D. Loffreda, D. Simon and P. Sautet, *Surf. Sci.*, 1999, **425**, 68–80.

Published on 08 September 2022. Downloaded on 10/6/2022 1:29:36 PM.

 This journal is © the Owner Societies 2022